AIAA Journal
Vol. 47, No. 9, September 2009

Aero-Optic Distortion in Transonic and Hypersonic Turbulent Boundary Layers

Christopher M. Wyckham* and Alexander J. Smits†
Princeton University, Princeton, New Jersey 08544

DOI: 10.2514/1.41453

A two-dimensional Shack–Hartmann wave-front sensor is used to study aero-optic distortion in turbulent boundary layers at transonic and hypersonic speeds, with and without gas injection. The large-scale motions in the outer layer, of the order of the boundary-layer thickness in size, are shown to dominate the aero-optic distortion. Gas injection always reduced the Strehl ratio, with helium injection generally giving lower Strehl ratios than nitrogen injection. The large aperture approximation is shown to be accurate for a wide variety of aberrations regardless of Mach number and gas injection. A new scaling argument for the root-mean-square phase distortion is proposed that appears to collapse the data better than previous models.

Nomenclature

C_B = constant defined by Eq. (20), $\frac{\mathrm{OPD}_{\mathrm{rms}}}{K_{GD}\rho_e\delta^* M_e^2 (u'_{\mathrm{rms}}/U_e)_{\mathrm{rms}}}$
C_f = skin friction coefficient
C_w = constant defined by Eq. (16), $\frac{\mathrm{OPD}_{\mathrm{rms}} r_2^{3/2}}{K_{GD}\rho_e\delta M_e^2 \sqrt{C_f}}$
I = intensity
K_{GD} = Galdstone–Dale constant
M = Mach number
n = index of refraction
p = pressure
Re_θ = Reynolds number based on freestream values and θ
r = recovery factor
r_1 = U_i/U_e
r_2 = T_i/T_e
r_3 = constant defined by Eq. (14), $(\sqrt{\frac{\rho\overline{u'^2}}{\tau_w}})_{0.5}/(\sqrt{\frac{\rho\overline{u'^2}}{\tau_w}})_i$
T = temperature
t = time
U = velocity in the streamwise direction
x = streamwise distance
y = wall-normal distance from the flat plate model
z = spanwise distance
γ = ratio of specific heats
δ = 99% boundary-layer thickness
δ^* = displacement thickness
θ = momentum thickness
Λ = integral length scale
λ = wavelength of light
ν = kinematic viscosity
ρ = density
ρ_{SL} = sea level density in a standard atmosphere
τ = shear stress

Subscripts

e = freestream value
i = intermediate value
rms = root mean square value
w = value at the wall
0 = maximum value

Superscripts

$\overline{(\;)}$ = mean value
$'$ = fluctuation from the mean

I. Introduction

AERO-OPTICS is the study of the interaction between light and air. More specifically, it is the study and measurement of the distortion of light propagating through an index of refraction field which is thin with respect to the imaging (or projecting) aperture. In high-speed flow, aero-optic degradation arises from density gradients across shock waves and from density fluctuations in free shear layers and turbulent boundary layers. In imaging applications, the image becomes blurred by the distortion, reducing the effective resolution. For optical targeting sensors, aero-optical degradation can lead to errors in the target location (bore-sight error, that is, the difference between the actual target position and its perceived position), reduced sensitivity, and the apparent breakup of a single target into multiple targets. In applications requiring the projection of energy, the peak irradiance on the target or receiving communications link can be seriously degraded. Here we use a Shack–Hartmann sensor to measure the two-dimensional distortion of wave fronts propagating through boundary layers at transonic and hypersonic Mach numbers, with and without gas injection, to learn more about the aero-optics of compressible turbulent boundary layers.

II. Background

Consider the transmission of light through a thin field of varying density fluid such as a turbulent boundary layer. The index of refraction of a fluid n varies linearly with density ρ according to the Gladstone–Dale equation

$$n = 1 + \rho K_{\mathrm{GD}} \tag{1}$$

where K_{GD} is the Gladstone–Dale "constant" which is a function of the type of fluid and the wavelength of light [1]. K_{GD} for air at visible wavelengths is approximately $2.27 \times 10^{-4}\ \mathrm{m}^3/\mathrm{kg}$. After traversing an index of refraction field in the y direction from y_1 to y_2, the variation in the absolute optical path length (OPL) for an initially flat wave front can be computed using

$$\mathrm{OPL}\,(x, z, t) = \int_{y_1}^{y_2} n(x, y, z, t)\mathrm{d}y \tag{2}$$

Presented as Paper 4775 at the 35th AIAA Plasmadynamics and Lasers Conference, Toronto, Ontario, Canada, 6–9 June 2005; received 7 October 2008; accepted for publication 20 May 2009.

*Graduate Student, Mechanical and Aerospace Engineering Department. Member AIAA.

†Professor, Mechanical and Aerospace Engineering Department. Fellow AIAA.

In most cases, the optical path difference (OPD) is the quantity of interest rather than the optical path length, where

$$\mathrm{OPD}\,(x,z,t) = \mathrm{OPL}(x,z,t) - \langle \mathrm{OPL}(x,z,t) \rangle \tag{3}$$

and the angle brackets denote the spatial average.

In a compressible boundary layer, the density ρ, temperature T, pressure p, and velocity U vary in space and time. Only the density fluctuations are relevant to optical distortions. The density fluctuations can be related to the velocity fluctuations using the strong Reynolds analogy (SRA) and the ideal gas law. The SRA links temperature fluctuations to velocity fluctuations in a turbulent boundary layer on an adiabatic plate according to

$$\frac{T'}{\bar{T}} = -(\gamma - 1)M^2 \frac{u'}{\bar{U}} \tag{4}$$

where γ is the specific heat ratio and M is the Mach number [2]. Primes indicate fluctuating quantities and overbars indicate local mean quantities. The SRA has been experimentally validated for Mach numbers as high as three, but remains useful for higher Mach numbers [3]. It is widely used in turbulence modeling for compressible wall-bounded turbulent flows [2].

A reasonable estimate of the pressure fluctuation level in a boundary layer is given by the rms value of the wall pressure fluctuation. In a zero pressure-gradient adiabatic layer at Mach 1.8, for example, Dussauge [4] found that $p'/\bar{p}_w = 1.0\%$ at the wall and about 0.2% in the freestream. In the bulk of the layer they found that $T'/\bar{T}$ was closer to 5%, indicating that the pressure fluctuations were considerably smaller than the temperature fluctuations. In a similar flow at Mach 2.85, Dolling and Murphy [5] found that $p'_w/\bar{p}_w$ was also about 1.0%, and Gibson and Dolling [6] show that at Mach 4.95 this ratio has a value of about 0.9%, suggesting that it does not change much with Mach number. Measurements at higher Mach numbers are more difficult and although Wang et al. [7] in a shock wave boundary-layer interaction at Mach 7.8 seem to show a value of about 4%, it is not clear their measurements were made sufficiently upstream of the shock to be in the undisturbed boundary-layer upstream, and the data may also have been contaminated by tunnel noise.

Accepting that the pressure fluctuations are small, the ideal gas law for small fluctuations leads to the result

$$\frac{\rho'}{\bar{\rho}} = (\gamma - 1)M^2 \frac{u'}{\bar{U}} \tag{5}$$

Equations (4) and (5) indicate that the density and temperature fluctuations are expected to be out of phase. This is in contrast to what is expected in isentropic flows, but experiments indicate that Eqs. (4) and (5) are a good approximation for zero pressure-gradient, adiabatic, supersonic turbulent boundary layers (see, for example, Smith and Smits [8]). (For additional discussion, see Smits and Dussauge [2].) Equation (5) illustrates the strong dependence of the density fluctuations on Mach number and mean density, indicating that aero-optical distortions are expected to increase at higher Mach numbers and lower altitudes.

The rms optical path difference can be estimated from flow variables such as the magnitude of the density fluctuations ρ' and the Eulerian integral scale Λ (a measure of the large-scale turbulent motions) by the linking equation suggested by Steinmetz [9]:

$$\mathrm{OPD}^2_{\mathrm{rms}} = 2K^2_{\mathrm{GD}} \int_0^L \overline{\rho'^2(y)}\Lambda(y)\mathrm{d}y \tag{6}$$

(see, for example, Buell [10]). The linking equation assumes that the density fluctuations are random and normally distributed and that the integration length L is much greater than the integral scale Λ.

In the inner region of a turbulent boundary layer, the structures tend to organize into long, streamwise streaks with a characteristic spacing of $100\nu_w/u_\tau$, where ν_w is the kinematic viscosity at the wall, τ_w is the wall shear stress, and $u_\tau = \sqrt{\tau_w/\rho_w}$ is the friction velocity. The inner region extends to approximately 10–15% of the boundary-layer thickness δ. Within this region, structures convect at approximately the mean velocity at the height of the structure. The outer region of the boundary layer is dominated by structures sometimes termed large-scale motions (LSMs). These structures are defined by large intrusions of irrotational freestream fluid deep into the boundary layer. The size of LSMs is of the same order as the boundary-layer thickness and they convect with a velocity somewhat less than the edge or freestream velocity U_e (typically $0.8U_e$) [3].

Because the phase distortion is integrated through the boundary layer, the contributions from the larger scale structures in the outer region would be expected to be significant. However, Eq. (6) shows that the variation of relative density fluctuations with height above the wall must also be taken into account. The density fluctuations are stronger in the inner half of the boundary layer, but in a compressible flow the local density decreases sharply close to the wall, especially in high Mach number flows. Hence, there has been some controversy over which region dominates the phase distortion. For example, Sutton [11] argued that structure sizes on the order of 0.1δ were of greatest importance, but Masson et al. [12] noted the marked effect of intermittency due to LSMs in their analysis of Gilbert's KC-135 data [13].

When an initially planar phase front propagates through a boundary layer, and the aperture is greater than the structures of interest, the wave front will carry the imprint of the aero-optically important structures. Also, because the inner and outer region structures convect at different velocities, a time-resolved series of wave fronts can be used to determine the propagation speed and therefore the origin of the aero-optically active structures in the boundary layer. In this respect, Buckner et al. [14] report a streamwise correlation length of 0.75δ and streamwise velocity of $0.81U_e$ for a Mach 0.5 turbulent boundary layer, suggesting that in their experiment the LSMs were the most important structures contributing to aero-optic distortion.

Two figures of merit are often used to describe the degree of aberration in a wave front: the root-mean-square variation across the wave front, or ϕ_{rms}, and the Strehl ratio (SR), defined as the ratio of the measured irradiance $I(t)$ in the far field to the diffraction limited theoretical maximum I_0. That is,

$$\mathrm{SR}\,(t) = \frac{I(t)}{I_0} \tag{7}$$

The Strehl ratio is a measure of the far-field impact of the wave-front aberration and is of particular interest in the design of an optical system.

There are two definitions of SR in common use. Some researchers (for example, Jumper and Fitzgerald [15]) specify that the SR is calculated at a fixed point (the centerline), while others (for example, Mani et al. [16]) calculate SR at the point of maximum irradiance, regardless of its location, which may be more representative of the quality of the spot. We call the first definition SR_c and the second SR_m. For a far-field spot with high irradiance but a small bore-sight error, $\mathrm{SR}_c < \mathrm{SR}_m$. Even if bore-sight error is compensated (as it is in all of our calculations), an image that is broken up into more than one peak will have a low value of SR_c.

If the exact wave-front shape is known, it is possible to calculate the far field using Fourier optics. It is often useful, however, to be able to estimate the Strehl ratio using the rms optical path difference $\mathrm{OPD}_{\mathrm{rms}}$ and the wavelength of the light λ. The large aperture approximation (LAA) provides this estimate by assuming that the aperture is much larger than the dimension of the phase aberrating structures and that the phase at any point on the wave front follows a Gaussian distribution in the spanwise and streamwise directions [9]. The LAA suggests

$$\mathrm{SR} = \exp\left(-\left(\frac{2\pi \mathrm{OPD}_{\mathrm{rms}}}{\lambda}\right)^2\right) \tag{8}$$

If the large-scale motions dominate the aberrated phase shape in a boundary layer, the largest scale of the phase aberrations will be approximately equal to the boundary-layer thickness. The LAA will then be valid if the aperture is much greater than δ for boundary-layer flows.

The implementation of the LAA will also depend on the definition of the Strehl ratio. Steinmetz [9] used the maximum irradiance (SR_m), not the centerline irradiance (SR_c). As noted, the difference can be significant. Cicchiello and Jumper [17] questioned the validity of the large aperture approximation for the specific case of a two-dimensional heated jet. They used SR_c instead of SR_m, and because their wave fronts tended to break up into multiple peaks due to the nature of the wave fronts produced by their flow, they reported lower Strehl ratios. They found an average SR_c of 0.265 compared to predictions based on the large aperture approximation of 0.88. When they removed the wave-front tilt (which moves the location of the far-field peak without affecting its amplitude), their estimated Strehl ratio increased to 0.43.

Only a relatively small number of experiments have measured wave fronts in compressible, turbulent boundary layers. At transonic speeds, Gilbert [13] and Kelsall [18] used a shearing interferometer to measure the difference between two uncorrelated wave fronts after traversing the boundary layers of a KC-135 and a Learjet, respectively. The rms optical path difference was then inferred from this difference. Their experiments spanned Mach numbers from 0.25 to 0.57 at altitudes ranging from 0.3 to 12 km.

More recently, Gordeyev et al. [19] and Buckner et al. [14] studied wave-front aberrations due to turbulent boundary layers at Mach numbers from 0.42 to 0.92 using Malley probes. Malley probes propagate two laser beams through the flow and measure their displacements in the streamwise direction to determine the time series of the wave-front slopes at the location of each beam. A one-dimensional wave front is then reconstructed by assuming a frozen flow.

Even fewer studies of wave-front distortions due to flat plate boundary layers are available at hypersonic speeds. Most work at these Mach numbers has concentrated on seeker window technology for ballistic missile interceptors and has been performed on wedges instead of flat plates (see, for example, Willett et al. [20] and Marren [21]). The study by Yanta et al. [22] was performed on a turbulent boundary layer on a flat plate at Mach 7 and a unit Reynolds number of $9.6 \times 10^6\ \mathrm{m}^{-1}$. The Reynolds number at the window was not reported. Although 75 high resolution, two-dimensional wave fronts were obtained using a Shack–Hartmann sensor, only the Strehl ratios estimated by using the LAA were reported.

Sensor windows on hypersonic vehicles generally need to be cooled to protect them from the extreme temperature environment of atmospheric flight. Most commonly a coolant gas such as helium is injected into the boundary layer, which significantly degrades the aero-optic performance of the system [23]. Etz [24] and Auvity et al. [25] found that helium injection under certain conditions introduces regular, streamwise features into a hypersonic boundary layer which were conjectured to be counter-rotating vortices. These steady features have important implications for an optical system. If the stable features suppress the random features in the turbulent boundary layer in whole or in part, their effect on the wave front can then be removed with low temporal bandwidth adaptive optics with a resulting improvement in the Strehl ratio.

In the research reported here, a Shack–Hartmann sensor was used to measure the two-dimensional distortion of wave fronts propagating through boundary layers at transonic and hypersonic Mach numbers. The data were used to investigate whether large- or small-scale motions dominate the shape of the wave front, to evaluate the large aperture approximation, and to validate the scaling argument presented below. The ability of adaptive optics coupled with helium injection to reduce wave-front distortions was also assessed.

III. Scaling of Aero-optic Aberrations

In the absence of a general scaling law for aero-optic distortion due to turbulent, compressible boundary layers, it is not possible to compare phase front aberration data taken under different flow conditions. As a result the design of airborne optical systems relies heavily on computational fluid dynamics, wind-tunnel tests, and/or flight tests. All three of these tools were required by Levy et al. [26], for example, in the design of a pod for long range aerial photography.

Gilbert [13], on the basis of his KC-135 data, proposed that the mean square value of the the OPD scaled linearly with the dynamic pressure and $\delta^{4/3}$. Kelsall [18], based on an analysis of his aircraft boundary-layer data, concluded that "There is clearly no simple rule-of-thumb answer to estimating the degradation in a light beam propagated through the aerodynamic boundary layer of an aircraft." Masson et al. [12] argued by way of the SRA that ϕ_{rms} should scale with $\rho_e M_e^2$, where the subscript denotes conditions at the edge of the boundary layer. Using a least-squares fit to Gilbert's data, they found that

$$\mathrm{OPD}_{\mathrm{rms}} = 2.20\lambda \left(\frac{\rho_e}{\rho_{\mathrm{SL}}} M_e^2 \right)^{1.16} \tag{9}$$

where ρ_{SL} is the sea level density in a standard atmosphere.

Alternatively, Buckner et al. [14] assumed that the density fluctuations in the boundary layer are due to the decreased pressure in vortex cores, and proposed that

$$\mathrm{OPD}_{\mathrm{rms}} = 4.6 K_{\mathrm{GD}} \rho_e M_e^2 \delta^* \left(\frac{u'_{\mathrm{rms}}}{U_e} \right)_{\mathrm{max}} \tag{10}$$

where δ^* is the displacement thickness of the boundary layer. This relation successfully collapsed their transonic boundary-layer data, although the rms phase level was overestimated by a factor of about 4.

A new scaling argument may be developed by using known scaling laws for compressible, turbulent boundary layers. We begin with Eq. (2) for a boundary layer of thickness δ:

$$\mathrm{OPL} = \int_0^\delta n(y)\,\mathrm{d}y$$

Using Eq. (1) and (3), we obtain

$$\mathrm{OPD} = \int_0^\delta n'\,\mathrm{d}y = \int_0^\delta K_{\mathrm{GD}} \rho'\,\mathrm{d}y \tag{11}$$

The SRA [Eq. (5)] then gives

$$\frac{\mathrm{OPD}}{K_{\mathrm{GD}} \rho_e} = \int_0^\delta (\gamma - 1) M^2 \frac{\rho}{\rho_e} \frac{u'}{U}\,\mathrm{d}y \tag{12}$$

where the overbars have been left off the mean quantities for clarity. Using $p = \rho R T$ with $p = p_e = \mathrm{const}$ (as expected for a boundary layer), we obtain

$$\frac{\mathrm{OPD}}{K_{\mathrm{GD}} \rho_e} = \int_0^\delta (\gamma - 1) M^2 \frac{T_e}{T} \frac{u'}{U}\,\mathrm{d}y = \int_0^\delta (\gamma - 1) M^2 \sqrt{\frac{C_f}{2}} \left(\frac{U_e T_e}{U T} \sqrt{\frac{\rho_e}{\rho}} \right) \sqrt{\frac{\rho u'^2}{\tau_w}}\,\mathrm{d}y \tag{13}$$

where the skin friction coefficient $C_f = 2\tau_w/(\rho_e U_e^2)$.

Equation (13) is now modeled to give an estimate for the rms phase difference by assuming that we can use intermediate values (values that have been averaged in some sense over the boundary-layer thickness) as an approximation to the integral. This argument is similar to the intermediate temperature concept used to develop skin friction relationships for compressible boundary layers [2]. Hence, for high Reynolds number flows where we expect the aero-optic distortion to depend largely on the outer layer structures, we propose

$$\frac{\mathrm{OPD}_{\mathrm{rms}}}{K_{\mathrm{GD}} \rho_e \delta} \approx (\gamma - 1) M_i^2 \sqrt{\frac{C_f}{2}} \left[\frac{U_e T_e}{U_i T_i} \sqrt{\frac{\rho_e}{\rho_i}} \right] \left(\sqrt{\frac{\rho \bar{u}'^2}{\tau_w}} \right)_i$$

where the subscript i denotes intermediate values. We now assume that

$$\frac{\mathrm{OPD_{rms}}}{K_G \rho_e \delta} = (\gamma - 1) M_e^2 \frac{r_1}{r_2^{3/2} r_3} \sqrt{\frac{C_f}{2}} \left(\sqrt{\frac{\rho \overline{u'^2}}{\tau_w}} \right)_{0.5}$$

where $U_i = r_1 U_e$, $T_i = r_2 T_e$, $M_i^2 = (r_1^2/r_2) M_e^2$, and we relate the nondimensional intermediate turbulence intensity to its value at $y/\delta = 0.5$ according to

$$\left(\sqrt{\frac{\rho \overline{u'^2}}{\tau_w}} \right)_{0.5} = r_3 \left(\sqrt{\frac{\rho \overline{u'^2}}{\tau_w}} \right)_i \tag{14}$$

The parameters r_0, r_1, and r_3 are expected to be close to unity. Note that r_1 and r_2 are not independent because they are connected through the total temperature variation across the boundary layer and the usual isentropic relationships in the freestream. For an adiabatic wall, we find $T_e/T_i = 1/r_2$, so that

$$r_2 = 1 + \frac{\gamma - 1}{2} M_e^2 (1 - r_1^2 r)$$

where r is the recovery factor ($r \approx 0.9$). For a nonadiabatic wall, we make the simplest assumption $T_i = (T_w + T_e)/2$ so that

$$r_2 = \frac{1}{2} \left(\frac{T_w}{T_e} + 1 \right)$$

Finally,

$$\frac{\mathrm{OPD_{rms}}}{K_{\mathrm{GD}} \rho_e \delta} = C_w r_2^{-3/2} M_e^2 \sqrt{C_f} \tag{15}$$

where

$$C_w = (\gamma - 1) \frac{r_1}{r_3 \sqrt{2}} \left(\sqrt{\frac{\rho \overline{u'^2}}{\tau_w}} \right)_{0.5} \tag{16}$$

If we assume that $r_1 \approx 0.8$ (the convective speed of the large-scale motions), and $r_3 \approx 1$, and use the fact that

$$\left(\sqrt{\frac{\rho \overline{u'^2}}{\tau_w}} \right)_{0.5} \approx 1.5$$

at all Mach numbers, independent of Reynolds number [2], then with $\gamma = 1.4$ we expect $C_w \approx 0.34$.

Note that the scaling proposed by Buckner et al. [14] [Eq. (10)] may be written in a similar form to Eq. (15) by putting $C_w = C'_w$, where

$$C'_w = \frac{4.6}{\sqrt{C_f}} r_2^{3/2} \sqrt{\frac{T}{T_e} \frac{\delta^*}{\delta}} \left(\sqrt{\frac{\rho \overline{u'^2}}{\tau_w}} \right)_{\max} \tag{17}$$

It is clear that C'_w is not a constant because it will, among other things, depend on heat transfer.

The coefficient C_w can be estimated from previous data if the other quantities in Eq. (15) are known. Gilbert [13] provides only the aircraft altitude and Mach number, the values of δ and $\mathrm{OPD_{rms}}$, and the x location where the data were taken. His data span altitudes from 300 m to 10.7 km and Mach numbers from 0.25 to 0.57. The aircraft skin was measured to behave as an adiabatic wall. The skin friction coefficient can be estimated using the correlations given by Smits and Dussauge [2], and if the freestream density follows the standard atmosphere, and a power law is used to estimate Re_x, we find that for each of his seven experiments C_w ranges from 0.09 to 0.31. The value of C_w seems to decrease for increasing δ, but this may be an artifact of the assumptions made in estimating the missing flow variables (density and Reynolds number).

Gordeyev et al. [19] provide seven more data points in transonic boundary layers for Mach numbers ranging from 0.42 to 0.93. They do not provide Re_x, and they report the displacement thickness δ^* instead of δ. However, the flow conditions may be estimated by assuming isentropic flow and an adiabatic wall, and a standard sea level stagnation density for their in-draft tunnel. A virtual origin for x can then be found by fitting the δ^* distribution to a power law. Under these assumptions, their values for C_w range from 0.20 to 0.32.

Even with the broad assumptions required to compute C_w from these previous studies, the results are encouraging. Below, we will use our data sets to further investigate the scaling expressed by Eq. (15).

IV. Experimental Procedures

Only a brief summary of the experimental procedures and data analysis will be presented here. Further details are given by Wyckham et al. [27] and Wyckham [28].

The transonic and hypersonic wind tunnels used for this research were supplied by the same compressed air system. The air from a bank of eight reciprocating compressors was dried and filtered and stored in four pressure vessels with a total capacity of 60 m^3 and a working pressure of 17 MPa. The stagnation pressure, stagnation temperature, and static pressure were measured and the Mach and Reynolds numbers were calculated assuming isentropic conditions in the core flow.

A common test section was used for both tunnels. The test section is cylindrical with an inner diameter of 0.23 m and with four large, rectangular access ports used for mounting models and permitting optical access (Fig. 1).

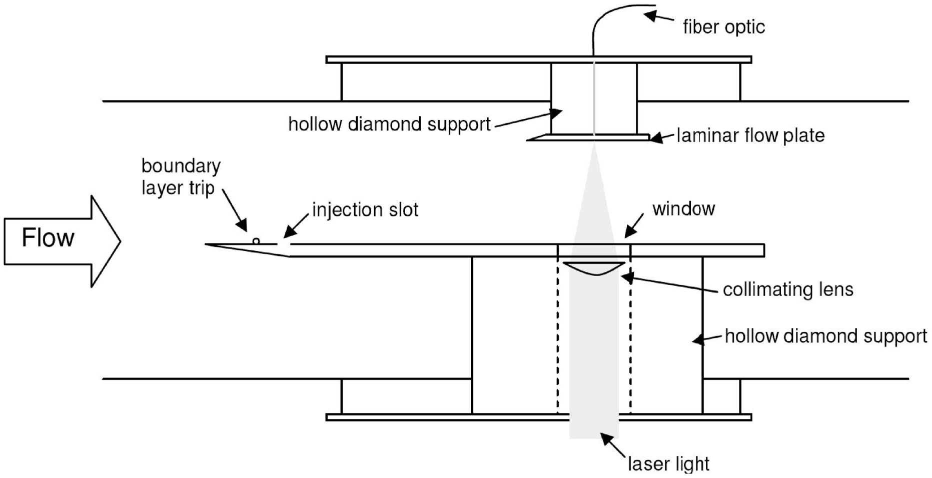

Fig. 1 Side view of the two flat plate models showing their relative orientation when installed in the test section.

The transonic facility is a simple blowdown tunnel. The stagnation pressure is controlled by an automated control valve. From the valve, the air flows into a large stagnation chamber, then through a smooth contraction with an area ratio of approximately 40:1 to the test section before exiting to the atmosphere via a muffler. The Mach number is controlled by varying the stagnation pressure so that Mach number and Reynolds number cannot be varied independently. At our operating Mach number of approximately 0.78, the tunnel Reynolds number was 18×10^6 m^{-1}. The static pressure is equivalent to that at an altitude of approximately 1000 m in the standard atmosphere.

In the hypersonic wind-tunnel facility, the supply air is throttled down from the supply pressure via a control valve and then enters a resistively heated piping coil to bring the air to the desired stagnation temperature. A two-stage ejector system is used to reduce the pressure downstream of the nozzle to a minimum of 3.4 kPa absolute. Maximum run time is approximately 2.5 min with both ejectors running. Further details on the hypersonic facility are given by Baumgartner [29]. Typical stagnation conditions were 9.2 MPa and 700 K. The unit Reynolds number for our operating conditions was approximately 18×10^6 m^{-1} (the same as in the transonic experiments). The static pressure is equivalent to an altitude of roughly 30,000 m in the standard atmosphere.

No attempt was made to control the model temperature other than to avoid damaging the optical components due to high temperatures. The plate temperature was measured using a thermocouple fixed just under the surface and the wall temperature was 0.50 of the adiabatic wall temperature for all hypersonic flow conditions.

In the work presented here, a Shack–Hartmann sensor was used to measure two-dimensional wave fronts. An expanded laser beam passes through the flow and an array of lenslets focuses a grid of spots onto a digital camera, as shown in Fig. 2. Each spot is projected onto a position normal to the local average wave-front slope across that lenslet. The wave-front slope is measured at a number of points and the phase shape of the distorted wave front is then reconstructed from the slopes.

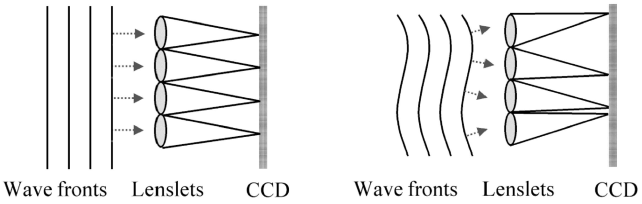

Fig. 2 Operating principle of a Shack–Hartmann sensor. Left: plane wave front. Right: aberrated wave front, showing the corresponding movement of the spots.

Two flat plate models were constructed: a main boundary-layer plate and a laminar flow plate. Figure 1 shows the test section arrangement. Each plate is supported by a hollow diamond-shaped support.

The small laminar flow plate is designed to launch the laser light into the tunnel without it passing through the tunnel wall turbulent boundary layer. The plate is 6.4 mm thick, 200 mm long, and 75 mm wide. It has a 10 deg leading edge. The 0.75-mm-diam laser exit hole is located on the centerline 120 mm from the leading edge. The plate is positioned with the top face approximately 75 mm from the tunnel centerline to ensure that the tunnel boundary layer passes below the plate.

The main boundary-layer flat plate model is 470×150 mm^2 and 12.7 mm thick. As with the laminar flow plate, the leading edge has a 10 deg angle. A 2.4-mm-diam circular trip wire was placed 59 mm from the leading edge.

The effects of gas injection on the aero-optic performance of the boundary layer were investigated by injecting nitrogen or helium transverse to the flow through a slot in the flat plate. The slot measured 1×25.4 mm^2 and it was located 70 mm from the leading edge. The width of the slot in the streamwise direction could be varied by the use of shims. The injection parameter used was the momentum ratio J which compares the momentum flux in the main flow to the momentum flux of the jet

$$J = \frac{(\rho U^2)_{\mathrm{jet}}}{(\rho U^2)_e} = \frac{(\gamma p M^2)_{\mathrm{jet}}}{(\gamma p M^2)_e} \tag{18}$$

To gather the light transmitted through the boundary layer, the main flat plate model is fitted with a 51-mm-diam circular fused silica window located on the centerline, with its center 356 mm from the leading edge. The diamond-shaped support has a matching 51 mm hole for the light to pass through. A lens is situated inside this hole, just under the window, to collimate the light. A second, smaller bore hole in the support strut carries instrumentation leads and injection gas. The gas passes up through the plate via a machined channel to the slot near the front of the plate. The channel also serves as a stagnation chamber for the injected gas. The plate temperature and static pressure are measured just upstream of the window, and the stagnation temperature and pressure of the injection gas is measured within the channel.

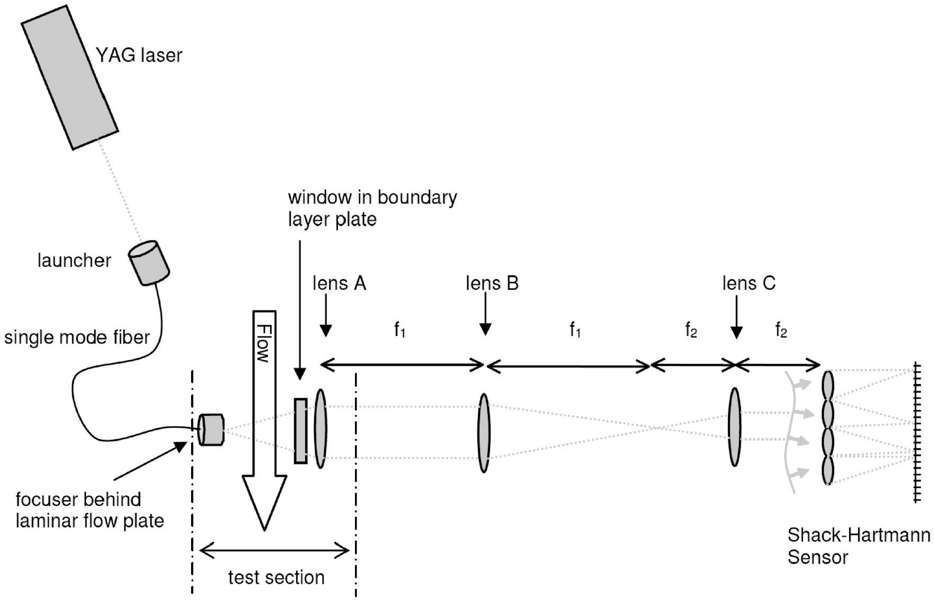

Fig. 3 Optical arrangement.

The overall optical arrangement is shown in Fig. 3. A continuous wave, frequency doubled Nd-YAG laser with a wavelength of 532 nm is used as the light source.

To reduce the effects of mechanical vibration, the laser light is introduced into the tunnel using an optical fiber. The laser is coupled into a single mode optical fiber using a commercial launcher from Oz Optics. The light is then focused to a spot by a custom dual element focuser, mounted on the back of the laminar flow plate. The focal point coincides with the hole in the plate, and the light diverges as it crosses the gap between the two plates. As it passes through the window in the boundary-layer plate, a spherical aberration is introduced because the off-axis rays pass through the window at an angle whereas the on-axis rays do not.

After passing through the window in the main test plate, the light passes through three plano-convex lenses (A, B, and C in Fig. 3). The first lens collimates the light. The other two lenses are arranged in a $4f$ lens system which eliminates the diffraction of the signal with propagation distance by exploiting the Fourier transforming property of lenses [30]. A focal length ratio for the two lenses of approximately 2.5:1 was used so that the image of the entire window diameter was accommodated on the camera chip. This focal length ratio also amplifies the wave-front slopes by a factor of 2.5, increasing the sensor sensitivity.

After the $4f$ lens system, the light is focused onto the camera by the lenslet array, a square array of 400-μm-diam lenses with a focal length of 71 mm. Although the array has 65×65 lenslets, only 17×17 lenslets were used in this configuration.

The camera was a Redlake HGLE high-speed digital CMOS camera operated with resolutions of 752×1128 pixels at 1000 fps, 752×752 at 1500 fps, and 256×256 at 5000 fps. All of the two-dimensional wave fronts were captured at 1500 fps. Pixels are 12 μm across with a 45% fill factor, and the camera outputs 8-bit gray-scale images. An integrated electronic shutter allows integration times as short as 5 μs. The camera is also capable of a "line" resolution mode, 20×1128 pixels at 50,000 fps, which is fast enough to allow time-resolved one-dimensional wave fronts to be captured in transonic flow.

The output of the Shack–Hartmann sensor is a series of digital images showing a grid of spots. These images are manipulated and compared to calibration images to produce a representation of the aberrated wave front. All data analysis was performed using MATLAB.

A series of calibration pictures (taken with no flow) are first averaged together to minimize random noise. Because the apparatus has an inherent spherical aberration, the calibration spots are not evenly spaced or aligned on a square grid. An automated, adaptive routine is used to find the location of the spots and the size of the region around each spot where the program will later search the experimental images for the displaced spot. The centroid of each calibration spot is then found and stored.

For each image taken during an experiment, the new spot centroid locations are found to subpixel accuracy using a least-squares fit to a Gaussian surface and compared to the calibration locations to produce the average slope of the wave front in the spanwise and streamwise directions at each lenslet. These slopes are then used to construct a biquadratic surface representing the phase of the laser light after passing through the boundary layer. This surface is found by using a least-squares fit and singular value decomposition. The least-squares fit was weighted by the calculated uncertainty on each slope. Using Monte Carlo simulations, Wyckham [28] showed that this procedure improves the quality of the fit by 60%.

The resulting wave fronts are postprocessed in three ways. First, the mean phase for each individual wave front is set to zero because it is arbitrary. Second, any vibrations in the system will tend to move the lenslet array as a unit so that every spot moves the same amount in the same direction, producing a tilt in the wave front. This tilt is removed by least squares fitting a plane to the wave front and then subtracting it from the data. Third, the spherical aberration inherent to the system is removed by averaging together all of the phase fronts and then fitting a paraboloid to the result. A paraboloid is used instead of a sphere because it is much faster to process and leads to the same degree of accuracy. The paraboloid is then subtracted from each phase.

Table 1 Experimental conditions

	M_∞	M_{jet}	Re_x	Re_{jet}	J
Transonic					
1-D no injection	0.78	N/A	6.3×10^6	N/A	N/A
No injection	0.79	N/A	6.4×10^6	N/A	N/A
Narrow N_2	0.77	0.25	6.4×10^6	1800	0.12
Narrow He	0.77	0.24	6.5×10^6	610	0.11
Wide N_2	0.77	0.24	6.5×10^6	5500	0.11
Wide He	0.75	0.23	6.3×10^6	2000	0.12
High J He	0.78	0.44	6.5×10^6	3700	0.38
Hypersonic					
No injection	7.7	N/A	6.2×10^6	N/A	N/A
N_2 injection	7.8	1	5.9×10^6	2200	0.12
He injection	7.6	1	7.0×10^6	790	0.12

After postprocessing, the far field of each phase front is found using a fast Fourier transform (FFT). The Strehl ratio can then be found by comparison with the FFT of a planar wave front.

V. Results and Discussion

Ten different experimental conditions were investigated, as outlined in Table 1. The full data set is presented by Wyckham [28], and only a selection of the final data will be presented here. One thousand wave fronts were measured in each case. In the first experiment listed in the table, the Shack–Hartmann sensor was used in a one-dimensional mode. All other experiments were performed using the two-dimensional mode.

As can be seen from Table 1, data were taken in hypersonic and transonic flow, and with no injection, nitrogen injection, and helium injection. In all injection cases except the "high J helium" case, the injection momentum ratio J was held constant. The jet Reynolds number was computed based on the slot width (in the narrow, streamwise direction) and was varied at constant J by varying the slot width. All hypersonic injection cases, the high J helium case, and the transonic injection cases labeled "wide slot," used a 1-mm-wide injection slot. The two transonic injection cases labeled "narrow slot" used a 0.33-mm-wide slot. The slot length in the spanwise direction was held constant.

The boundary-layer thickness δ is used to normalize the streamwise and spanwise dimensions. For the hypersonic cases, Baumgartner [29] found $\delta = 11.5$ mm under similar flow conditions. For the transonic case, the boundary-layer thickness was not measured, but because it was only used as a scaling parameter it was estimated using a one-seventh power law [2], which gave $\delta \approx 5.7$ mm. Its value has no effect on the Strehl ratio measurements.

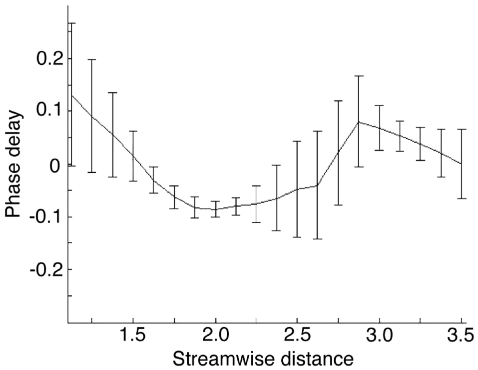

Fig. 4 Output of a one-dimensional Shack–Hartmann sensor, including uncertainties. The streamwise distance is normalized by the boundary-layer thickness. Values on both axes are approximate.

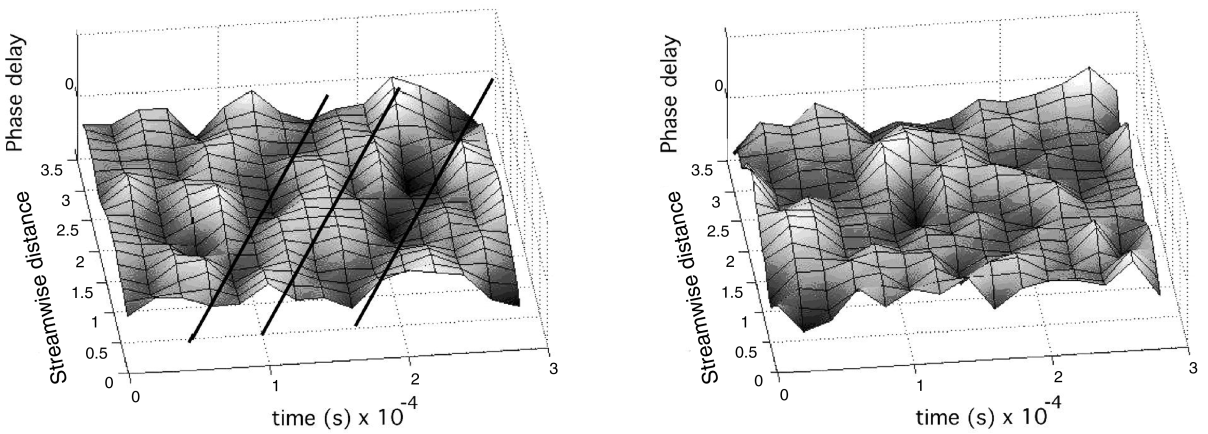

Fig. 5 Waterfall plot of one-dimensional wave-front data from a transonic boundary layer with helium injection. Phase delay = $\mathrm{OPD}_{\mathrm{rms}}/\lambda$. Left: Experimental data. Right: Random slopes. Phase delay axis is not calibrated. The streamwise distance is normalized by the boundary-layer thickness.

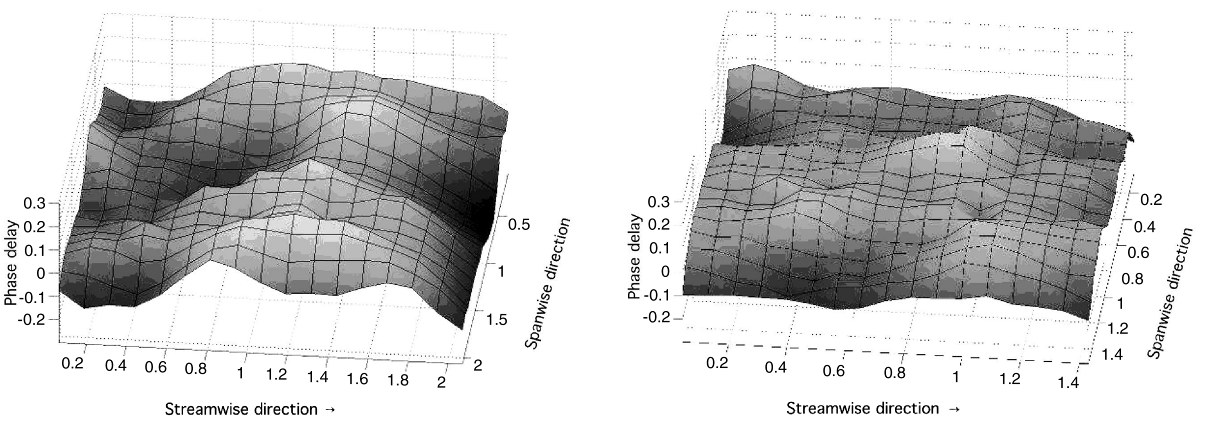

Fig. 6 Typical wave fronts with no gas injection. Left: Transonic flow. Right: Hypersonic flow. Streamwise and spanwise distances normalized by boundary-layer thickness.

A. One-Dimensional Results

The framing rate of the Redlake camera at high resolutions is too low to capture full, time-resolved two-dimensional phase fronts for the flow velocities considered here. However, a single line of spots in the streamwise direction can be imaged at over 50 kHz. A structure moving at the freestream velocity would take five frames to traverse the aperture at this frame rate. The result is a one-dimensional slice through the phase sheet.

Figure 4 shows a typical result. The uncertainties give a signal-to-noise ratio of order 1. The two-dimensional phase reconstruction technique uses twice as many equations as unknowns, whereas the one-dimensional reconstruction technique uses only one more equation than unknowns. As a result, random noise is more important in the one-dimensional case than in the two-dimensional case.

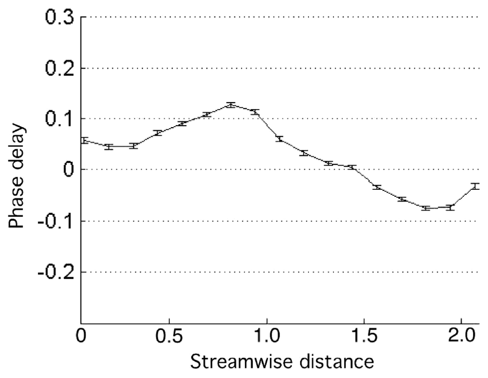

Fig. 7 Typical uncertainties on a one-dimensional slice through the data. Transonic flow with no injection. The streamwise distance is normalized by the boundary-layer thickness.

A "waterfall plot" is created by stacking a time series of one-dimensional streamwise wave-front slices side by side. One of the horizontal axes is therefore time and the other is space in the streamwise direction. A structure moving past the aperture will describe a diagonal trajectory on the waterfall plot.

The left side of Fig. 5 shows a waterfall plot of measured data. The superimposed lines in the figure indicate the trajectory of a structure moving at the freestream velocity. The slopes of the ridges and valleys indicate that the aberrating structures travel at a velocity equal to or slightly less than the freestream velocity. These structures are, therefore, large-scale motions in the outer region of the boundary layer. The right side of Fig. 5 shows a waterfall plot of a signal created from wave-front slopes randomly sampled from a population equivalent in mean and variance to the experimental data. The amplitude of the resulting random waterfall plot is similar to the experimental data, but the diagonal structures are no longer present.

B. Two-Dimensional Shack–Hartmann Results

Typical wave fronts with no injection are shown in Fig. 6, one for transonic flow and one for hypersonic flow. Note that the "phase delay" is the nondimensional optical path difference = $\mathrm{OPD}_{\mathrm{rms}}/\lambda$. The uncertainties are represented as error bars in Fig. 7. As expected, these uncertainties are considerably smaller than those for the one-dimensional results shown in Fig. 4. The uncertainties shown are only the random uncertainties and do not include constant biases such as errors in the dimensions of the sensor because these biases would only represent a constant scale factor in the data. The analysis probably underestimates the uncertainty because it assumes

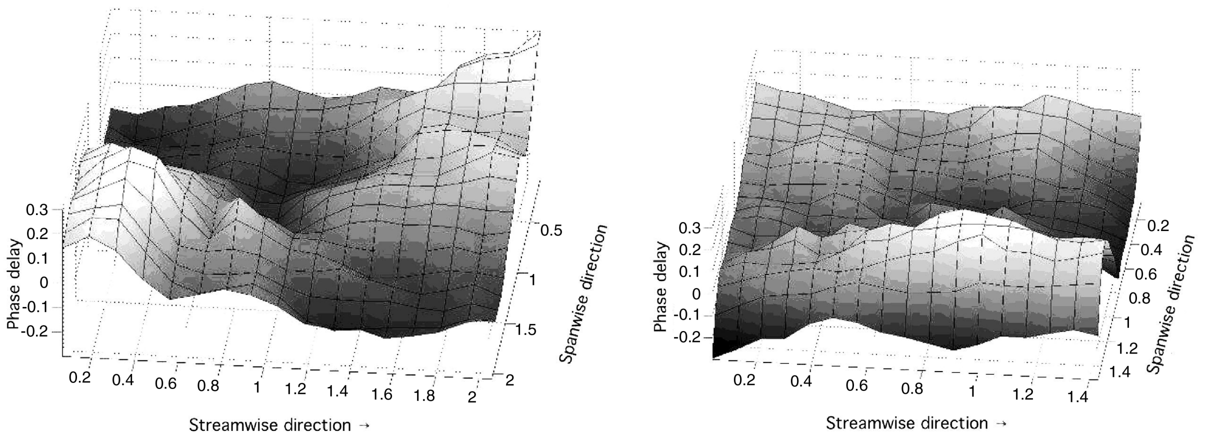

Fig. 8 Typical wave fronts with helium injection ($J = 0.12$, wide injection slot). Left: transonic flow. Right: hypersonic flow. Streamwise and spanwise distances are normalized by the boundary-layer thickness.

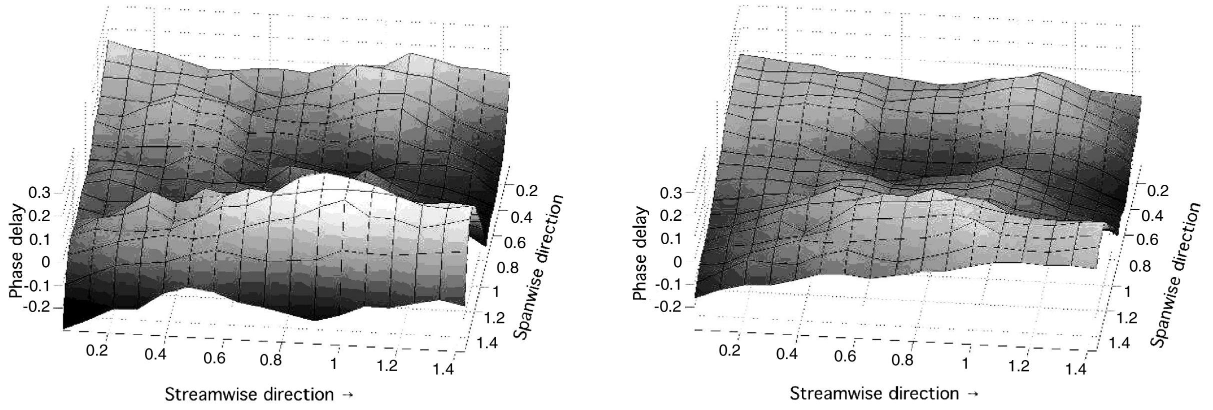

Fig. 9 Effect of simulated fixed adaptive optics for helium injection under hypersonic flow conditions ($J = 0.12$, wide injection slot). Left: instantaneous wave front. Right: fluctuating component of the same wave front, representing the wave front as corrected by fixed adaptive optics. Streamwise and spanwise distances are normalized by the boundary-layer thickness.

Gaussian spots, whereas some of the spots certainly deviate significantly from this ideal.

Figure 8 shows wave fronts with helium injection under transonic and hypersonic flow conditions ($J = 0.12$, wide injection slot). Distinct streamwise structures are visible in the hypersonic case but not in the transonic case. Figure 9 shows the effect of subtracting the mean of 1000 wave fronts from the hypersonic injection case so that only the fluctuating component is shown. This subtraction of the mean simulates a fixed adaptive optic system designed to remove the mean value of the signal.

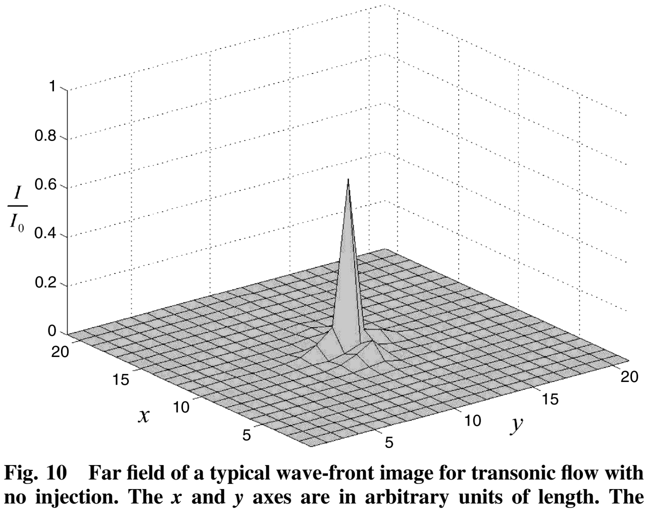

Fig. 10 Far field of a typical wave-front image for transonic flow with no injection. The x and y axes are in arbitrary units of length. The corresponding Strehl ratio is 0.691 ± 0.008.

The far field of each wave front was calculated by taking the square of the Fourier transform of the transfer function $f = \exp(2\pi i \mathrm{OPD}/\lambda)$. Figure 10 shows a typical far field. The Strehl ratio was then found by comparing the peak intensity of the aberrated far field to that of a planar wave front. The results, plotted against the large aperture approximation, are shown in Fig. 11. The agreement is remarkable in all cases, even for Strehl ratios as low as 0.2 to 0.3, below which there is probably little practical interest.

The spatial frequency content of the wave fronts was found by computing the power spectral density (PSD) for each data set. A Welch window was used to prevent the edge effects from corrupting the data [31].

For each data set, the average PSD was found over the 17,000 samples constituting the data set for both the streamwise and spanwise directions.

Figure 12 shows that for the transonic case the streamwise and spanwise spectra are nearly identical. Although the frequency bins are rather broad, the spectra peak at a spatial frequency of around $0.5/\delta$, which would be expected for a structure size of roughly one δ (a feature of size δ) diameter would be fitted by a sinusoid with a wavelength of two δ, that is, a frequency of $0.5/\delta$.

Most importantly, the PSD approaches zero well within the sampling window, indicating that the spatial sampling frequency of the Shack–Hartmann sensor was sufficient to resolve the important large-scale motions.

Figure 13 shows the PSDs for the hypersonic flow. The spanwise frequency peaks at a value somewhere less than $1/\delta$, but the

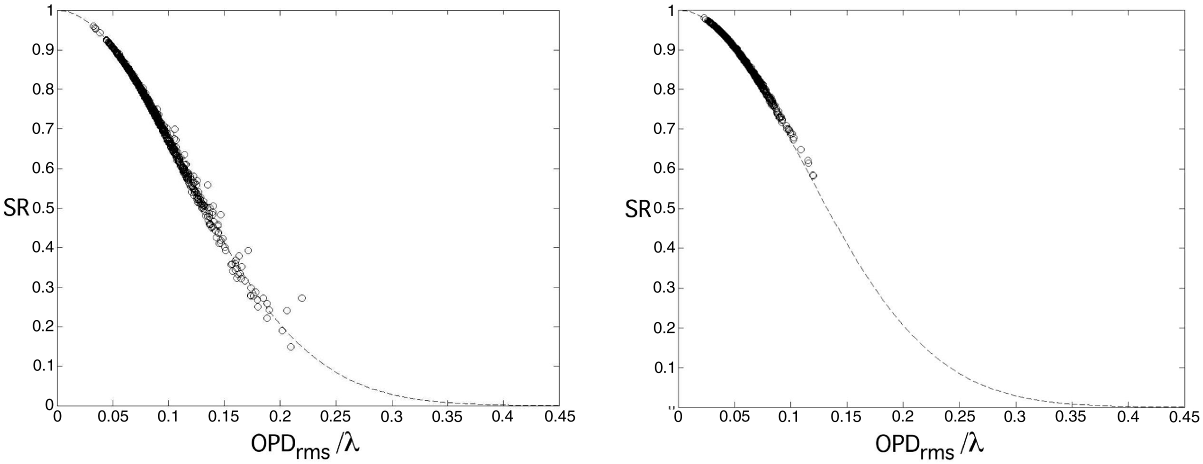

Fig. 11 Relationship between the rms optical path difference $\mathrm{OPD}_{\mathrm{rms}}$ and the Strehl ratio SR compared with the large aperture approximation (LAA) given by Eq. (8) (no gas injection). Left: transonic flow. Right: hypersonic flow. Open circles: measurements; dashed lines: LAA.

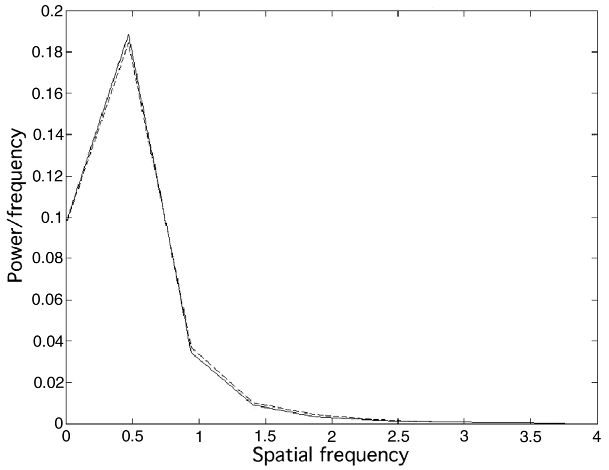

Fig. 12 Power spectral density (arbitrary units) for transonic flow with no gas injection. Streamwise direction: solid line; spanwise direction: dashed line. The spatial frequency is normalized by the boundary-layer thickness.

streamwise frequency peaks at a much higher value. As will be seen later, the data for the hypersonic cases were corrupted by large vibrations and no conclusions about the nature of the turbulence can reliably be made from the PSD plots.

The minimum resolvable scale is set by the spacing between the lenses in the sensor array, and the maximum resolvable scale is set by the overall size of the array. The $4f$ lens system allows a tradeoff to be made between the maximum and minimum allowable frequencies. Figure 6 shows that with the $4f$ lens system used, the sensor can resolve structures up to approximately 2δ in the transonic flow and 1.4δ in the hypersonic flow. The sensor is insensitive to larger structures because tilt is removed from the signal in postprocessing.

Figure 13 shows that the lenslet spacing was small enough to resolve the smallest structures. Because the PSD tends toward zero as the Nyquist frequency is approached, smaller frequencies are not present in the signal. If the lenslet spacing was too large, the PSD would first decrease and then increase again as the Nyquist frequency was approached due to aliasing.

A large density structure will lift or depress a large area of the wave front, affecting the location of many spots on the Shack–Hartmann sensor in a correlated manner. The two-dimensional correlation contours were constructed by finding the correlation coefficients between the phase height values for the center spot and the phase height values for every other spot. The results, shown in Fig. 14, indicate that the average structure size in the transonic case was approximately 1.2δ and that the structures were reasonably symmetrical. The contours for the hypersonic flow are distorted in the streamwise direction due to a known vibrationally induced aberration. However, the average structure can be seen to extend roughly 1δ in the spanwise direction, providing another indication that the aero-optically important structures are the large-scale motions in the outer region of the boundary layer.

Table 2 summarizes the mean and standard deviation of the rms phase height and Strehl ratios for each experiment, using both the total wave front and the fluctuating component alone (the total wave front minus the mean of all wave fronts). It is important to note that

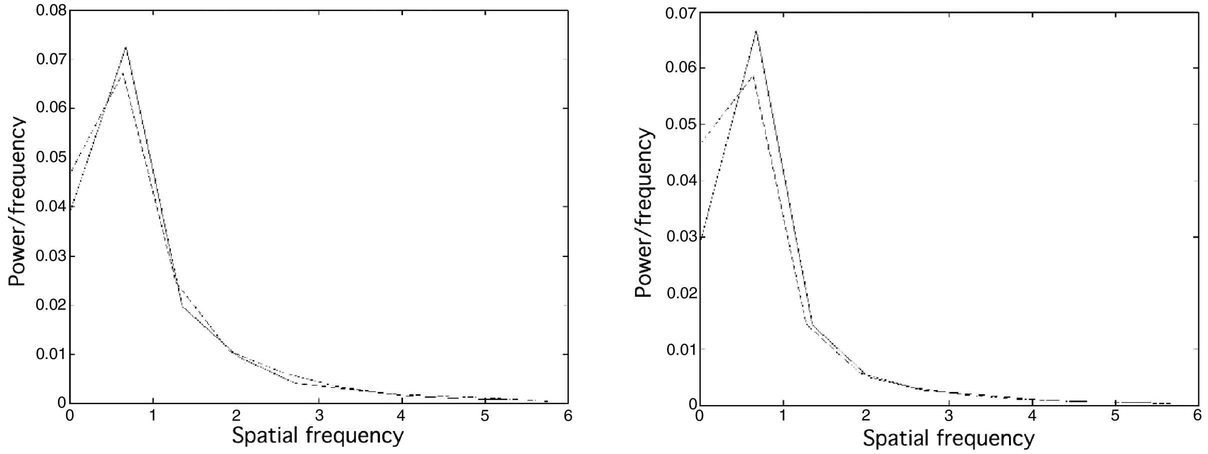

Fig. 13 Power spectral density (arbitrary units) for hypersonic flow with no gas injection. The spatial frequency is normalized by the boundary-layer thickness. Left: total wave front; right: fluctuating component. Streamwise direction: solid lines; spanwise direction: dashed lines.

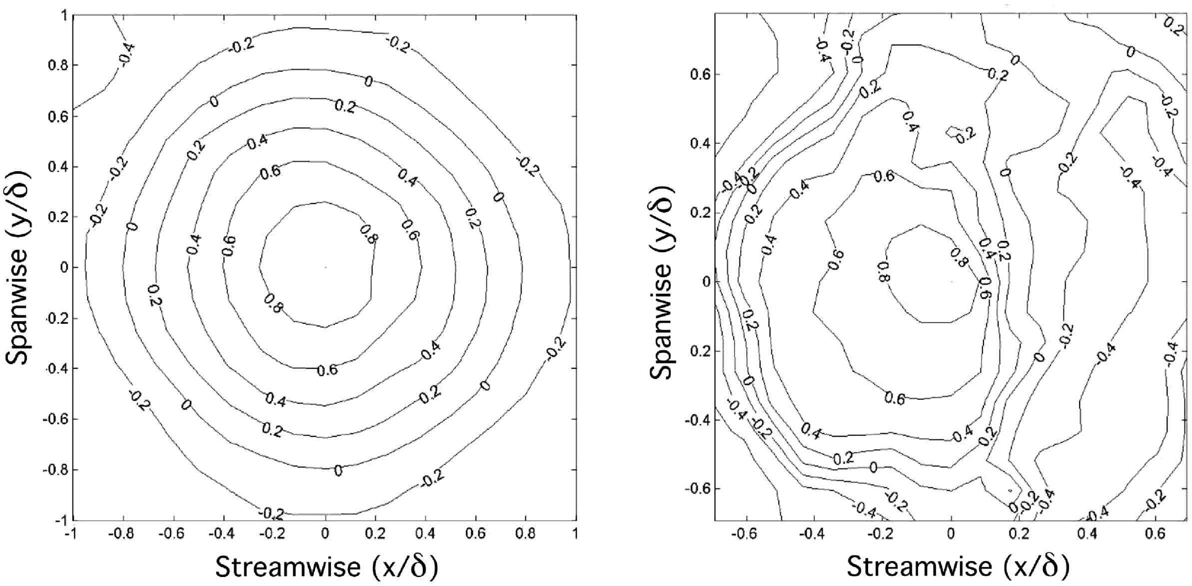

Fig. 14 Correlation contours of phase delay with no gas injection. Left: transonic flow; right: hypersonic flow.

the standard deviation is not an uncertainty, but rather a measure of how much variance there is from frame to frame.

Only marginal improvements in the Strehl ratio were obtained by subtracting the mean wave front for all cases except the hypersonic helium injection case. In that case, a 14% improvement was seen, bringing the Strehl ratio up to approximately the same level as the nitrogen injection case, but still short of the no injection case. For the helium injection case, the standard deviation is 13% lower than in the no injection case and 39% lower than in the nitrogen injection case.

VI. Test of New Scaling

Equation (15) can be written as

$$C_w = \frac{\mathrm{OPD}_{\mathrm{rms}} r_2^{3/2}}{K_{\mathrm{GD}} \rho_e \delta M_e^2 \sqrt{C_f}} \tag{19}$$

If this relationship holds, we expect C_w to be a universal constant over all flow conditions. With no gas injection, we found $C_w = 1.0$ for the transonic case, and $C_w = 0.7$ for the hypersonic case. These numbers are in reasonable agreement with the estimated value of 0.34, but, more important, the relatively small variation found in C_w over the Mach number range from 0.8 to 7.8 is very encouraging.

Similarly, we can test the scaling proposed by Buckner et al. [14] by writing Eq. (10) as

$$C_B = \frac{\mathrm{OPD}_{\mathrm{rms}}}{K_{\mathrm{GD}} \rho_e M_e^2 \delta^* (u'_{\mathrm{rms}}/U_e)_{\max}} \tag{20}$$

where $C_B = 4.6$ according to Buckner et al. To find C_B for our data, we used $\delta^* \approx \delta/8 = 5.7/8 = 0.71$ mm for the transonic case according to a one-seventh power law, and $\delta^* = 6$ mm for the hypersonic case as measured by Baumgartner [29]. The maximum turbulence intensity was estimated to be 0.08 for the transonic flow and 0.045 for the hypersonic flow using the correlations given by Smits and Dussauge [2]. Equation (20) then gives $C_B = 4.4$ and 0.44 for the transonic and hypersonic flows, respectively. Buckner et al. [14] compute an expected value for C_B of 4.6, but their own transonic boundary-layer data yield a value of 1.2. This large variation in C_B suggests that their scaling is less universal than that expressed by Eq. (15).

VII. Conclusions

A Shack–Hartmann sensor sensitive enough to measure two-dimensional wave-front distortions due to compressible, turbulent boundary layers was developed. When used in a high-speed, one-dimensional mode, the sensor was able to resolve structures in a transonic flow as they propagated past the sensor, albeit with large uncertainties. These structures were observed to move at or slightly below the edge velocity, indicating that they were due to large-scale motions in the outer region of the boundary layer. This result agrees

Table 2 Mean and standard deviation σ of the rms variation in the nondimensional phase delay, $\mathrm{OPD}_{\mathrm{rms}}/\lambda$, and the Strehl ratio, SR. "Total wave front" is the output of the phase fitting routine, and "Fluctuating component" is the result after simulated adaptive optics have been applied

	Total wave front				Fluctuating component			
	$\mathrm{OPD}_{\mathrm{rms}}/\lambda$		SR		$\mathrm{OPD}_{\mathrm{rms}}/\lambda$		SR	
	Mean	σ	Mean	σ	Mean	σ	Mean	σ
Transonic								
No injection	0.088	0.027	0.732	0.135	0.086	0.028	0.739	0.137
Narrow N_2	0.085	0.027	0.745	0.131	0.085	0.028	0.749	0.132
Narrow He	0.099	0.028	0.678	0.139	0.098	0.028	0.681	0.140
Wide N_2	0.094	0.029	0.703	0.139	0.092	0.029	0.713	0.140
Wide He	0.125	0.031	0.543	0.154	0.123	0.031	0.553	0.152
High J He	0.196	0.052	0.283	0.138	0.196	0.052	0.285	0.139
Hypersonic								
No injection	0.058	0.015	0.872	0.059	0.052	0.016	0.893	0.062
N_2 injection	0.067	0.019	0.836	0.084	0.063	0.021	0.850	0.088
He injection	0.085	0.011	0.755	0.051	0.061	0.013	0.860	0.054

with the conclusion formed by Buckner et al. [14] using a Malley probe in transonic flows.

The correlation contours of the phase distortion for the case of transonic flow with no injection demonstrate that the aero-optically important structures are slightly more than 1δ in size, again indicating that the dominant aberrations are due to large-scale motions.

Although the hypersonic data were contaminated by significant mechanical vibrations, the aero-optic data in the helium injection case revealed streamwise structures that were steady in time, confirming the observations of Auvity et al. [25] obtained using Rayleigh scattering. Helium injection reduced the Strehl ratio, but when the mean was subtracted from the individual wave fronts the Strehl ratio increased to approximately that of the nitrogen injection case. If helium injection is required for window cooling, it would seem advantageous to ensure that the injection is done in such a way as to produce these longitudinal structures so that a low temporal bandwidth adaptive optic system can be used to correct for the known distortions. However, if no cooling is required, better performance can be achieved by avoiding gas injection.

The large aperture approximation was shown to be accurate for a wide variety of aberrations regardless of Mach number and the presence or absence of gas injection. Only when the Strehl ratio fell below 0.2 or 0.3 did the LAA underestimate the Strehl ratio. However, even if a system is being developed with very low anticipated Strehl ratios, the large aperture approximation can provide a worst case scenario. In fact, as shown by Wyckham [28], the large aperture approximation was found to apply even for small apertures as long as the tilt of the wave front is removed.

Finally, a new scaling argument for the rms phase distortion was found to give better results than previous proposals over a wide range of Mach numbers and flow conditions. Further experiments will be needed to establish its full range of applicability.

Acknowledgments

The support of U.S. Air Force Office of Scientific Research under grant F49620-02-1-0124 is gratefully acknowledged. Additional support was received under Small Business Innovation Research Phase I contract FA8650-04-M-3426.

References

[1] Merzkirch, W., *Flow Visualization*, 2nd ed., Academic Press, New York, 1985.

[2] Smits, A. J., and Dussauge, J.-P., *Turbulent Shear Layers in Supersonic Flow*, 2nd ed., Springer, New York, 2006.

[3] Spina, E. F., Smits, A. J., and Robinson, S. K., "The Physics of Supersonic Turbulent Boundary Layers," *Annual Review of Fluid Mechanics*, Vol. 26, No. 1, 1994, pp. 287–319. doi:10.1146/annurev.fl.26.010194.001443

[4] Dussauge, J.-P., "Rapport Convention," ONERA/IMST 20.352/SAT/CDC, 1986.

[5] Dolling, D. S., and Murphy, T. M., "Unsteadiness of the Separation Shock Wave Structure in a Supersonic Compressible Ramp Flowfield," *AIAA Journal*, Vol. 21, No. 12, 1983, pp. 1628–1634. doi:10.2514/3.60163

[6] Gibson, B. G., and Dolling, D. S., "Wall Pressure Fluctuations Near Separation in a Mach 5, Sharp Fin-Induced Turbulent Interaction," AIAA Paper 91-0646, 1991.

[7] Wang, S. F., Ren, Z. Y., and Wang, Y., "Effects of Mach Number on Turbulent Separation Behaviours Induced by Blunt Fin," *Experiments in Fluids*, Vol. 25, No. 4, 1998, pp. 347–351. doi:10.1007/s003480050239

[8] Smith, D. R., and Smits, A. J., "Simultaneous Measurement of Velocity and Temperature Fluctuations in the Boundary Layer of a Supersonic Flow," *Experimental Thermal and Fluid Science*, Vol. 7, No. 3, 1993, pp. 221–229. doi:10.1016/0894-1777(93)90005-4

[9] Steinmetz, W. J., "Second Moments of Optical Degradation due to a Thin Turbulent Layer," *Aero-Optical Phenomena, Progress in Astronautics and Aeronautics*, edited by K. G. Gilbert, and L. J. Otten, Vol. 80, AIAA, New York, 1982, pp. 78–100.

[10] Buell, D. A., "Overview of 6 × 6 Ft. Wind-Tunnel Aero-Optics Tests," *Aero-Optical Phenomena, Progress in Astronautics and Aeronautics*, edited by K. G. Gilbert, and L. J. Otten, Vol. 80, AIAA, New York, 1982, pp. 139–188.

[11] Sutton, G. W., "On Optical Imaging Through Aircraft Turbulent Boundary Layers," AIAA Paper 80-1413, 1980.

[12] Masson, B., Wissler, J., and McMackin, L., "Aero-Optical Study of a NC-135 Fuselage Boundary Layer," AIAA Paper 94-0277, 1994.

[13] Gilbert, K. G., "KC-135 Aero-Optical Turbulent Boundary-Layer/Shear-Layer Experiments," *Aero-Optical Phenomena, Progress in Astronautics and Aeronautics*, edited by K. G. Gilbert, and L. J. Otten, Vol. 80, AIAA, New York, 1982, pp. 306–324.

[14] Buckner, A., Gordeyev, S., and Jumper, E. J., "Optical Aberrations Caused by Transonic Attached Boundary Layers: Underlying Flow Structure," AIAA Paper 2005-0752, 2005.

[15] Jumper, E. J., and Fitzgerald, E. J., "Recent Advances in Aero-Optics," *Progress in Aerospace Sciences*, Vol. 37, No. 3, 2001, pp. 299–339. doi:10.1016/S0376-0421(01)00008-2

[16] Mani, A., Wang, M., and Moin, P., "Computational Study of Aero-Optical Distortion by Turbulent Wake," AIAA Paper 2005-4655, 2005.

[17] Cicchiello, J. M., and Jumper, E. J., "Far-Field Optical Degradation due to Near-Field transmission Through a Turbulent Heated Jet," *Applied Optics*, Vol. 36, No. 25, 1997, pp. 6441–6452. doi:10.1364/AO.36.006441

[18] Kelsall, D., "Optical Measurements of Degradation in Aircraft Boundary Layers," *Aero-Optical Phenomena, Progress in Astronautics and Aeronautics*, edited by K. G. Gilbert, and L. J. Otten, Vol. 80, AIAA, New York, 1982, pp. 261–293.

[19] Gordeyev, S., Jumper, E. J., Ng, T. T., and Cain, A. B., "Aero-Optical Characteristics of Compressible, Subsonic Turbulent Boundary Layers," AIAA Paper 2003-3606, 2003.

[20] Willet, R. A., Xerikos, J., and Grossman, J. J., "Hypersonic Wind Tunnel Measurements of Optical Signal Distortion due to Propagation Through Cooled-Window Mixing Layers," *Proceedings of SPIE*, SPIE–International Society for Optical Engineering, Bellingham, WA, 2005, pp. 103–115.

[21] Marren, D., "Aero-Optical Demonstration Test in the AEDC Hypervelocity Wind Tunnel 9," AIAA Paper 99-4544, 1999.

[22] Yanta, W. J., Spring, W. C., III, Lafferty, J. F., Collier, S. C., Bell, R. L., Neal, D., Hamrick, D., Copland, J., Pezzaniti, L., Banish, M., and Shaw, R., "Near-and Far-Field Measurements of Aero-Optical Effects due to Propagation Through Hypersonic Flows," AIAA Paper 2000-2357, 2000.

[23] Korejwo, H. A., and Holden, M. S., "Ground Test Facilities for Aerothermal and Aero-Optical Evaluation of Hypersonic Interceptors," AIAA Paper 92-1074, 1992.

[24] Etz, M. R., "The Effects of Transverse Sonic Gas Injection on a Hypersonic Boundary Layer," Ph.D. Thesis, Princeton University, Princeton, NJ, 1998.

[25] Auvity, B., Etz, M. R., and Smits, A. J., "Effects of Transverse Helium Injection on Hypersonic Boundary Layers," *Physics of Fluids*, Vol. 13, No. 10, 2001, pp. 3025–3032. doi:10.1063/1.1401813

[26] Levy, Y., Hornsteirn, M., and Lednicer, D. A., "Aerooptical Design of a Long-Range Oblique Photography Pod," *Journal of Aircraft*, Vol. 40, No. 3, 2003, pp. 516–522. doi:10.2514/2.3125

[27] Wyckham, C. M., Zaidi, S. H., Miles, R. B., and Smits, A. J., "Measurement of Aero-Optic Distortion in Transonic and Hypersonic, Turbulent Boundary Layers with Gas Injection," AIAA Paper 2005-4755, 2005.

[28] Wyckham, C. M., "Aero-Optic Characteristics of Turbulent Compressible Boundary Layers," Ph.D. Thesis, Princeton University, Princeton, NJ, 2006.

[29] Baumgartner, M. L., "Turbulence Structure in a Hypersonic Boundary Layer," Ph.D. Thesis, Princeton University, Princeton, NJ, 1997.

[30] Thurow, B., Samimy, M., and Lempert, W., "Simultaneous MHz Rate Flow Visualization and Wave-Front Sensing for Aero-Optics," AIAA Paper 2003-0684, 2003.

[31] Press, W. H., Flannery, B. P., Teukolsy, S. A., and Vetterling, W. T., *Numerical Recipes in Pascal*, Cambridge University Press, Cambridge, England, U.K., 1994.

N. Chokani
Associate Editor